https://doi.org/10.31436/iiumej.v27i2.4246

A Robust Low-Complexity Star Centroiding Algorithm for Autonomous Navigation under Lunar Noise Conditions

ANIS HANNANI RAZAMAN[1], YASSER ASRUL AHMAD[1*], TEDDY SURYA GUNAWAN[1], OTHMAN OMRAN KHALIFA[1], MILA POPOVIĆ[2]

[1]*Department of Electrical and Computer Engineering, International Islamic University Malaysia, Kuala Lumpur, Malaysia*
[2]*Astronomical Observatory Belgrade, Serbia*

**Corresponding author: yasser@iium.edu.my*

(Received: 27 February 2026; Accepted: 1 May 2026; Published online: 10 May 2026)

ABSTRACT: Star-based navigation on the lunar surface is severely degraded by strong regolith reflections, abrupt illumination transitions, and sensor-induced noise, all of which lower the signal-to-noise ratio (SNR) and impair centroiding accuracy. Existing methods address this trade-off poorly: classical center-of-mass (COM) and Gaussian fitting are computationally light but noise-sensitive, whereas iterative weighting and learning-based approaches improve accuracy at the cost of high computational load and large training data. This study addresses this gap by proposing a low-complexity yet robust star centroiding algorithm tailored for lunar-surface imagery. The pipeline integrates median filtering for impulse-noise suppression, an adaptive global threshold (set at 30% of peak intensity) for star-region segmentation, and an intensity-weighted COM estimator for sub-pixel localization. The method was implemented in MATLAB R2023b and evaluated on 30 Stellarium-derived star fields, each corrupted by Gaussian, Poisson, salt-and-pepper, speckle, and solar-glare noise spanning SNRs from −4.71 dB to 0.72 dB. Benchmarked against standard COM, Gaussian fitting, and the Sieve Search Algorithm (SSA), the proposed method achieves the lowest average root-mean-square error (RMSE = 1.218 pixels), the lowest Euclidean distance error (1.143 pixels), and the lowest false detection rate (FDR = 6.716%), corresponding to relative reductions of 21.5%, 16.7%, and 32.7% over the best baseline, respectively. The algorithm's favorable accuracy–complexity trade-off makes it well-suited for resource-constrained onboard processors in future lunar exploration and autonomous spacecraft navigation missions.

ABSTRAK: Navigasi berasaskan bintang di permukaan bulan terjejas dengan ketara akibat pantulan regolit yang kuat, perubahan pencahayaan yang mendadak, dan hingar daripada penderia, yang kesemuanya menurunkan nisbah isyarat kepada hingar (SNR) dan menjejaskan ketepatan penganggaran sentroid. Kaedah sedia ada gagal mengimbangi keseimbangan ini: kaedah pusat jisim (COM) klasik dan pemadanan Gaussian adalah ringan dari segi pengiraan tetapi sensitif terhadap hingar, manakala kaedah pemberat berulang dan berasaskan pembelajaran mesin meningkatkan ketepatan tetapi memerlukan beban pengiraan tinggi dan data latihan yang besar. Kajian ini mengisi jurang tersebut dengan mencadangkan satu algoritma penganggaran sentroid bintang yang teguh dan berkompleksiti rendah, khusus untuk imej permukaan bulan. Saluran pemprosesan menggabungkan penapisan median untuk menindas hingar impuls, ambang global mudah suai (ditetapkan pada 30% daripada keamatan puncak) untuk segmentasi kawasan bintang, dan penganggar COM berwajaran keamatan untuk penyetempatan subpiksel. Algoritma dilaksanakan dalam MATLAB R2023b dan dinilai ke atas 30 medan bintang Stellarium yang dicemari oleh hingar Gaussian, Poisson, garam-dan-lada, bintik, dan silau solar dengan SNR dari −4.71 dB hingga 0.72 dB. Berbanding COM standard, pemadanan Gaussian, dan Algoritma Carian Ayak (SSA), kaedah

yang dicadangkan mencapai purata RMSE terendah (1.218 piksel), jarak Euclidean terendah (1.143 piksel), dan kadar pengesanan palsu terendah (FDR = 6.716%), masing-masing mewakili pengurangan relatif 21.5%, 16.7%, dan 32.7% berbanding garis dasar terbaik. Imbangan ketepatan-kompleksiti yang baik menjadikan algoritma ini sesuai untuk pemproses dalam-pesawat dengan sumber terhad bagi misi penerokaan bulan dan navigasi pesawat angkasa autonomi pada masa hadapan.

KEYWORDS: *star centroiding, lunar navigation, harsh lunar environment, image processing, autonomous navigation.*

1. INTRODUCTION

Star sensors are essential components of autonomous spacecraft navigation. By identifying stellar patterns in captured images, they enable attitude determination with arc-second precision, providing a passive, drift-free reference that is independent of GPS, ground links, or planetary line-of-sight. Compared with celestial bodies such as Earth, the Sun, or the Moon, the abundance and angular stability of cataloged stars make them an ideal reference for orientation calculations [1]. With renewed international interest in lunar exploration, including missions under the International Lunar Research Station (ILRS) and the Turkish Lunar Mission [2], [3], [4], star-based navigation has re-emerged as a promising solution for surface and orbital operations. Historically, star trackers supported early lunar missions: the Apollo Command and Lunar Modules relied on optical star sightings for trajectory corrections and lunar descent navigation [5]. More recently, China's Chang'e-3 and Chang'e-4 landers used star trackers during transfer-orbit and lunar-orbit insertion phases, and the Queqiao relay satellite employed them to maintain Earth–Moon L2 halo orbit operations [6], [7].

Despite this heritage, the lunar surface remains an exceptionally hostile imaging environment for star sensors. The absence of an atmosphere, combined with strong solar reflection from the regolith, electrostatic dust levitation, and abrupt illumination transitions across the terminator, drives the SNR of star imagery into the negative-decibel regime, where centroiding errors and false detections rise sharply. Existing solutions lie at the two extremes of an unresolved trade-off. On one hand, classical centroiding methods such as the standard Center of Mass (COM), Gaussian fitting, and the recently proposed Sieve Search Algorithm (SSA) are computationally light and easy to implement, but degrade rapidly under low-SNR lunar conditions. On the other hand, learning-based and iterative-weighting methods improve robustness but at the cost of substantial computational load, parameter tuning, or large training datasets [8], [9], which are unattractive for the resource-constrained processors typically deployed on lunar landers and rovers.

To date, no published study has systematically benchmarked a low-complexity centroiding pipeline against multiple state-of-the-art baselines under a unified set of lunar-relevant noise models, including solar glare. This paper addresses that gap. The main contributions are threefold:

(i) a robust yet low-complexity centroiding pipeline integrating median filtering, an adaptive global threshold, and an intensity-weighted COM estimator, specifically tuned for lunar-surface imaging conditions;
(ii) a reproducible MATLAB-based evaluation framework using 30 Stellarium-derived star fields corrupted by five physically-motivated noise models (Gaussian, Poisson, salt-and-pepper, speckle, and solar glare) at SNRs ranging from −4.71 dB to 0.72 dB; and

https://doi.org/10.31436/iiumej.v27i2.4246

(iii) a quantitative comparison with COM, Gaussian fitting, and SSA, demonstrating consistent reductions in RMSE, Euclidean distance error, and false detection rate.

The remainder of this paper is organized as follows. Section 2 reviews the lunar imaging environment and prior centroiding methods. Section 3 details the proposed methodology and its MATLAB implementation. Section 4 presents the experimental results and critical analysis, and Section 5 concludes with directions for future work.

2. LITERATURE REVIEW

This section reviews the lunar imaging environment, the noise models commonly used to simulate it, and prior work on star detection and centroiding, identifying the limitations that motivate the proposed approach.

2.1. Moon Surface Environment

The lunar surface environment presents several physical and optical challenges that can affect the performance of star detection and centroiding for lunar-based navigation systems. The surface is mainly composed of two major geological regions: the highlands and the maria [10]. These variations in surface composition and reflectivity influence the background illumination captured by a star camera. The top layer, known as lunar regolith, is composed of fine dust, rock fragments, and glass particles produced by continuous micrometeoroid bombardment [11]. This regolith produces strong variations in reflection that contribute to background brightness and can interfere with star sensor imaging performance. The lunar regolith is present in the crust of the lunar layers, as shown in Figure 1, and the detailed sample of granular material that resembles dark, fine-grained sand or dirt is shown in Figure 2 [12], [13].

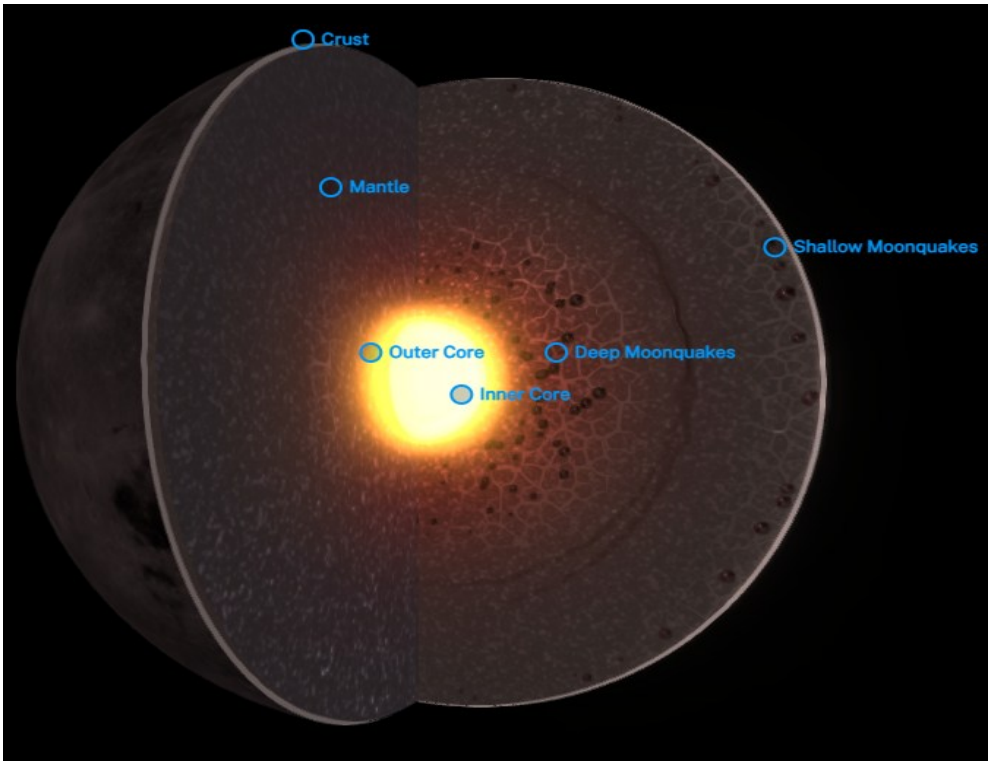

Figure 1. The regolith considered to be the uppermost layer of the lunar crust [13]

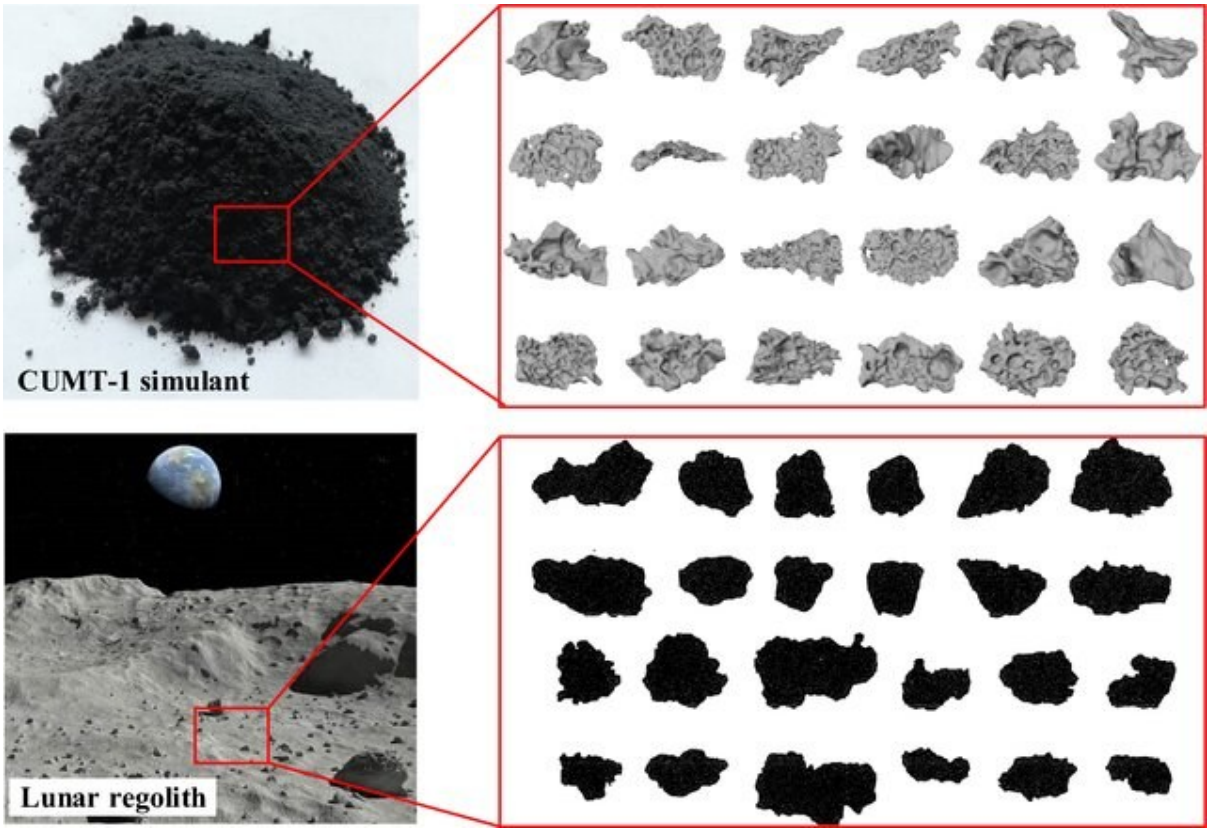

Figure 2. Detailed visualization of a lunar regolith simulant of CUMT-1 (China University of Mining and Technology-1) [12]

A defining characteristic of the lunar environment is the absence of a substantial atmosphere, so the sky remains completely black even during the day, with no atmospheric scattering. However, this condition also introduces several noise challenges. Sunlight reflecting off the regolith can generate glare, veiling luminance, and bright background gradients, all of which reduce the effective SNR for faint stars [14]. Additionally, electrostatic charging of lunar dust can lift particles above the surface, creating horizon glow and forward-scattering effects that introduce unwanted background illumination and intensity fluctuations in optical imaging systems [15], [16].

2.2. Different Types of Noise

The conditions outlined above translate into specific noise contributions that degrade star imagery. Faint stellar signals competing with strong, non-uniform regolith illumination, together with thermal and lighting extremes documented by NASA's Diviner instrument and the Apollo missions [17], [18], drive the captured SNR low, which directly reduces star visibility, increases false detections, and degrades centroid positional accuracy [19].

To recreate these lunar-surface challenges during algorithm development, several noise models are used to simulate degraded star fields. Table 1 describes the main noise types considered in this work, including Gaussian, Poisson, salt-and-pepper, and speckle noise [20], [21], [22], [23], as these represent common sensor- and photon-related disturbances in space imaging systems. Noise in digital images can generally be described as undesired brightness or color information, often visible as grainy texture or random intensity fluctuations [24]. Each

noise type arises from different physical or electronic mechanisms, and it is important to understand their properties for selecting appropriate noise reduction strategies.

Table 1. Noise and representations in the Lunar environment

Simulated Noises	Representations
Gaussian noise	Represents sensor electronic noise, such as thermal fluctuations in readout circuits, electronic sensor noise, and photon measurement randomness at low light levels.
Poisson noise	Simulates photon shot noise caused by the random nature of photon arrivals, which is amplified by the Moon's lack of atmosphere and the extreme contrast between illuminated and shadowed regions
Salt and pepper noise	Replicates impulse noise or high-contrast disruptions, specifically representing hardware/software failures, camera sensor defects, faulty pixels, or cosmic ray strikes
Speckle noise	Simulates multiplicative disturbances where noise scales with intensity, representing sensor gain fluctuations, optical imperfections, or rapid brightness changes caused by reflections from lunar dust or spacecraft surfaces
Light glare	Models intense solar reflections from the lunar regolith and direct solar illumination, which produce bright background gradients, veiling luminance, and structured light artifacts

2.3. Related Works on Star Detection

Two fundamental techniques used in image-based star detection are segmentation and centroiding. The segmentation technique removes background noise to isolate star information, and the centroiding technique is used to determine the precise positions of stars within an image [25], [26], [27]. These extracted positions are then utilized to estimate the orientation (attitude) of a spacecraft or satellite to enable precise navigation [28], [29].

Thresholding is the simplest and most widely used technique. It represents the first generation of low-level segmentation methods that rely on minimal prior information. Pixels with intensities above this threshold are classified as part of a star, while those below are treated as background noise [30], [31], [32]. According to Khalifa (2018), image segmentation involves grouping image regions that share similar characteristics to isolate relevant objects [24]. A recent study in medical imaging by Raman et al. introduced a mixed-thresholding and edge-preservation method to denoise MRI brain images while maintaining the important structural details in the medical image [33]. The thresholding dynamically responds to the noise characteristics, and next enables strong noise reduction without disturbing important image features [32], [34].

After the detection, the centroiding mechanism is applied to determine the precise location of each star. The process involves computing the intensity-weighted average of pixel positions within a star region, and finally results in a sub-pixel estimation of the star's center [35], [36], [37]. According to Liebe, the accuracy of a star tracker is strongly influenced by centroiding precision, particularly in the presence of image noise, pixel quantization effects, and optical distortions [19]. A novel technique, the Sieve Search Centroiding Algorithm (SSA) [38], improves accuracy by dividing images into smaller sub-regions and analyzing intensity distributions to compute the Center of Mass (COM). While it offers speed advantages over complex fitting algorithms, its sensitivity to noise and parameter variations remains a challenge. Figure 3 shows the graph of centroiding accuracy and the error curve from this study.

https://doi.org/10.31436/iiumej.v27i2.4246

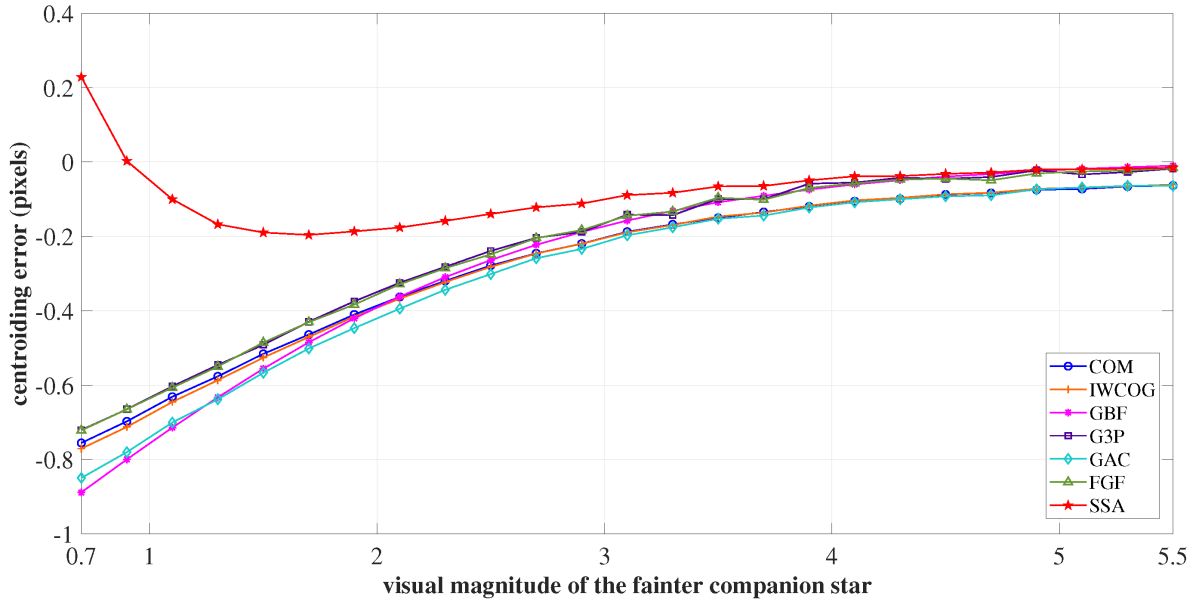

Figure 3. Centroiding error in estimating the brightness barycentre of an optical double-star pair [38]

Figure 4 illustrates how centroiding accuracy varies as the brightness barycentre shifts between the primary and secondary stars. When the secondary star is fainter than 4 VM (visual magnitude), most methods, including COM, Gaussian best fit (GBF), Gaussian three-point centroiding (G3P), Fast Gaussian Fitting (FGF), and SSA, estimate the centroid accurately, while iterative weighted center-of-gravity (IWCOG) and Gaussian Analytic Centroiding (GAC) show noticeable errors due to sensor noise and photo-electron spillover. While SSA is much faster than fitting methods, it is still inherently slower than the simplest grey-scale algorithms, such as COM or GAC.

A study introduced a dual-stage algorithm combining object segmentation and centroid extraction to eliminate non-stellar bright objects [26]. The primary contribution of this research is an effective pre-processing workflow designed to mitigate the challenge posed by non-stellar bright objects appearing in the star tracker's field of view. The centroiding technique proposed relies either on the Center of Gravity (CoG) or on locating the pixel of maximum intensity.

(a) (b) (c)

Figure 4. Centroiding results (a) star image with a big non-stellar bright object, (b) star position extraction by the first process, (c) star position extraction by the second process [26]

https://doi.org/10.31436/iiumej.v27i2.4246

Figure 4 provides a visual comparison of the results achieved by the proposed star centroiding algorithm, which includes steps to eliminate non-stellar, big-bright objects and extract star positions. The figures show the star number as the representation of the detected star blobs. Mahi et al. explicitly state that both proposed algorithms are limited in their ability to detect stars that are heavily affected by sunlight [26].

Zhao et al. (2024) proposed the Image Entropy-based Grayscale Iterative (IEGI) algorithm for extracting star spots from images affected by strong stray-light interference [9]. The method applies repeated grayscale iterations to suppress background noise based on local contrast information, followed by an object-to-pixel extraction stage that uses inner-outer templates and local image entropy to distinguish star regions from the background.

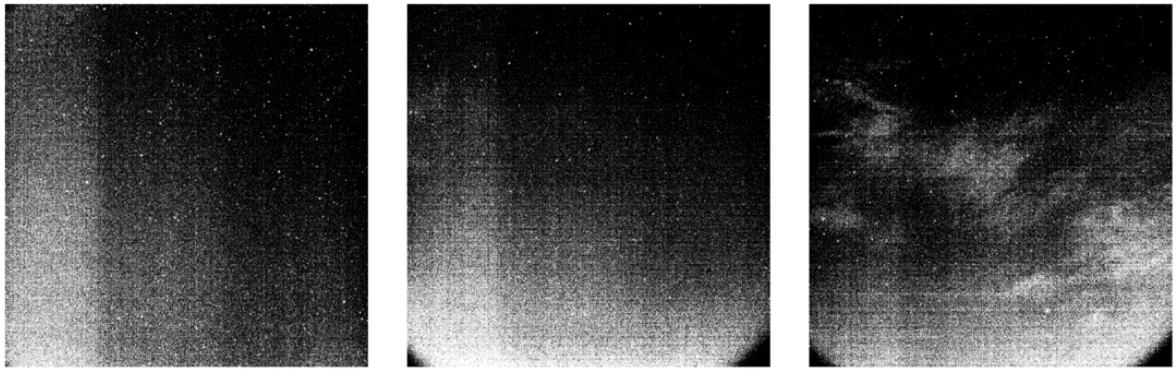

(a) (b) (c)

Figure 5. Real star image captured with the camera. (a) stray light condition 1; (b) stray light condition 2; (c) stray light condition 3 [9]

The study reported that the algorithm improved the star-detection rate by more than 45% compared to conventional max–mean filtering methods, while also reducing false detections by more than 50% relative to the Top-Hat transform. Experimental results with real star images showed that the method detected up to 93 star spots under severe interference conditions, where several conventional techniques failed. However, the iterative processing stages increase computational complexity, resulting in longer processing times of 0.69-1.04 seconds.

Table 2. Qualitative comparison of the related works

Method	Complexity	Computation Efficiency	Accuracy
SSA [38]	Moderate due to pattern-matching steps	Moderate but high in processing time	Good under moderate noise conditions
IEGI [9]	High	Low, it has a long running time due to the multiple iterations	High
1D CNN [8]	Low to Moderate	High with the use of sparse vectors allows skipping zero elements during convolution	High
Proposed	Moderate	Moderate to high	Improved robustness with lower complexity

Table 2 presents a qualitative comparison of several centroiding and star-detection methods in terms of computational complexity, efficiency, and detection accuracy. Based on the comparison table, more advanced methods, such as iterative weighting and entropy-based approaches, generally achieve higher accuracy and robustness, but they introduce greater computational complexity and longer processing times. The proposed method aims to provide

https://doi.org/10.31436/iiumej.v27i2.4246

a balance between computational simplicity and robust centroiding performance under low SNR lunar imaging conditions.

3. METHODOLOGY

The proposed centroiding pipeline consists of three sequential stages: (1) image preprocessing for noise suppression, (2) binary segmentation of candidate star regions, and (3) intensity-weighted centroid extraction. The complete workflow is illustrated in Figure 6. The algorithm was implemented in MATLAB R2025b on a workstation with an Intel Core i9-13900K CPU (32 cores), 64 GB DDR4 RAM, and Windows 11 Pro. The implementation relies on functions from the Image Processing Toolbox (`medfilt2`, `imbinarize`, `regionprops`, `bwlabel`) and the Computer Vision Toolbox; no GPU acceleration is required, which is consistent with the target deployment on resource-constrained onboard processors. To facilitate replication, all source images, generated noisy datasets, and processing scripts were organized in a single MATLAB project, with each noise model encapsulated in a dedicated function (`addGaussianNoise`, `addPoissonNoise`, `addSaltPepper`, `addSpeckle`, `addSolarGlare`).

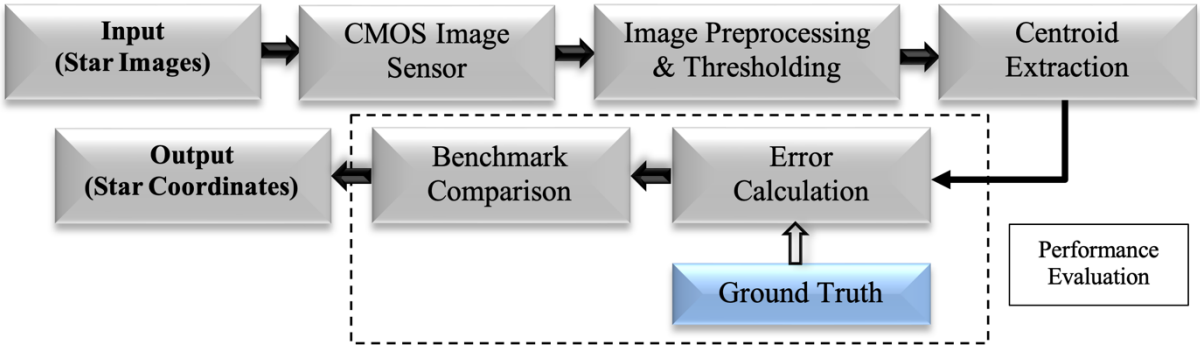

Figure 6. Block diagram of the proposed algorithm

A dataset of 30 star-field images was generated from the Stellarium Web online sky simulator [39]. Each image was exported as a PNG at 1920×1080 pixels (300 dpi) to emulate the field-of-view of a typical CMOS-based star camera. Camera calibration was excluded from the present study because consistent, clear-sky observations under local environmental conditions are difficult to obtain; this constraint is acknowledged in Section 5 as a direction for future work. Each clean image was then independently corrupted by five noise models (Gaussian, Poisson, salt-and-pepper, speckle, and a synthetic solar-glare gradient), producing a degraded dataset with measured SNRs ranging from −4.71 dB to 0.72 dB. The processing chain (median filter → threshold → centroid) was then applied to every image. Detected centroids were compared with the ground-truth coordinates extracted from the Stellarium star catalog, and three quantitative metrics were computed for each image: per-star Euclidean distance, root-mean-square error (RMSE), and false detection rate (FDR), as defined in Section 4.

3.1. Background Removal

A 3×3 median filter, implemented in MATLAB via the `medfilt2` function with symmetric boundary padding, is applied as the first preprocessing stage to suppress impulse-like noise without blurring star cores [40]. Within each 3×3 neighborhood, the central pixel is replaced by the median intensity, which preserves stellar peaks while removing isolated bright

https://doi.org/10.31436/iiumej.v27i2.4246

outliers caused by cosmic-ray hits, hot pixels, and salt-and-pepper sensor noise [41]. The 3×3 kernel size was selected after pilot tests with 3×3, 5×5, and 7×7 kernels: larger kernels were observed to over-smooth dim stellar peaks and shift their estimated locations, whereas the 3×3 kernel preserved sub-pixel peak structure while still effectively suppressing impulse noise. This sub-pixel preservation is critical because excessive smoothing biases the downstream centroid estimate.

As an example, consider a 3×3 pixel:

$$\begin{bmatrix} 34 & 36 & 40 \\ 38 & 255 & 41 \\ 35 & 39 & 37 \end{bmatrix}$$

The sorted values in the window are:

$$\{34, 35, 36, 37, \mathbf{38}, 39, 40, 41, 255\}$$

The median value is 38, which replaces the center pixel. The converted image becomes:

$$\begin{bmatrix} 34 & 36 & 40 \\ 38 & \mathbf{38} & 41 \\ 35 & 39 & 37 \end{bmatrix}$$

This method is then applied to the entire image to help produce cleaner star regions with preserved edges. This will allow subsequent detection and centroiding steps to operate more reliably under noisy imaging conditions.

3.2. Binary Segmentation

After median filtering, the denoised image is converted into a binary mask to isolate candidate stellar regions. A simple global thresholding scheme was selected over locally-adaptive methods (e.g., Otsu, Sauvola) because the lunar use case prioritizes deterministic, low-latency execution on embedded hardware [42], [43]. This segmentation is performed using a global threshold, T, which is defined as a fraction of the maximum intensity value in the image:

$$T = \alpha \cdot \max(I) \tag{1}$$

where I represents the pixel intensity, while α is a threshold factor ranging from 0 to 1 that controls the segmentation's sensitivity. The cutoff value T is a threshold factor in the range [0, 1] that controls segmentation sensitivity. To select an appropriate value, a sweep was performed over $\alpha \in \{0.2, 0.25, 0.3, 0.35, 0.4\}$ on the training subset. Values below 0.25 produced excessive false positives by retaining residual background noise, while values above 0.35 caused dim stars to be eliminated entirely. The setting $\alpha = 0.30$ minimized FDR without compromising recall and was therefore adopted for all subsequent experiments. Any pixel whose denoised intensity exceeds 30% of the per-image peak intensity is classified as a foreground (candidate-star) pixel; otherwise, it is classified as background. This binarization is expressed as:

$$B(x,y) = \begin{cases} 1, & if\ I(x,y) > T \\ 0, & otherwise \end{cases} \tag{2}$$

https://doi.org/10.31436/iiumej.v27i2.4246

In this formulation, $I(x, y)$ denotes the intensity of the pixel at position (x, y), and $B(x, y)$ is the resulting binary image. Foreground pixels $(B = 1)$ correspond to candidate star regions, whereas background pixels $(B = 0)$ represent noise and dark sky areas.

3.3. Centroid Extraction

Connected foreground regions in the binary mask are then labeled in MATLAB using the `bwlabel` function (8-connectivity) and filtered by area (minimum 3 pixels, maximum 200 pixels) to discard noise blobs and saturated artifacts. For each retained region, an intensity-weighted centroid is computed. In real star images, the captured intensity is non-uniform: brightness peaks near the stellar core and decays outward following an approximately Gaussian point-spread function. A simple binary centroid (geometric mean of mask pixels), therefore, introduces bias under noise, since it treats noisy boundary pixels and bright core pixels equally.

To address this, the COM formulation is applied, where pixel contributions are proportional to their intensities [44]. Concretely, the original (denoised) intensity image, the binary mask, and the labeled region map are passed to a custom MATLAB routine that, for each connected component, accumulates the intensity-weighted moments over the bounding box of the region; this gives a more stable, sub-pixel centroid estimate than equal weighting under low-SNR conditions.

The centroid coordinates are calculated as in Eq. (3):

$$x_c = \frac{\sum_{x,y} x \cdot I(x,y) \cdot w(x,y)}{\sum_{x,y} I(x,y) \cdot w(x,y)}, y_c = \frac{\sum_{x,y} y \cdot I(x,y) \cdot w(x,y)}{\sum_{x,y} I(x,y) \cdot w(x,y)} \quad (3)$$

where $I(x, y)$ is the pixel intensity at the coordinate (x, y), and the summation is taken over all pixels within the labeled star region.

4. Results and Discussion

This section reports the experimental evaluation of the proposed centroiding algorithm against three baselines (standard COM, Gaussian fitting, and SSA) on the 30-image dataset described in Section 3. Section 4.1 first characterizes the noise content and SNR distribution of the dataset; Section 4.2 then presents per-image and aggregate accuracy comparisons, supported by a critical discussion of failure modes and the practical implications of the observed performance gap.

4.1. Low SNR Star Images

Each clean image was independently corrupted by the five noise models defined in Table 1: Gaussian, Poisson, salt-and-pepper, speckle, and a synthetic solar-reflection (glare) gradient. SNR values were measured per image to characterize the severity of degradation, and the dataset was constructed to span mild-to-heavy noise conditions. Figure 7 shows the noise-free baseline used in all simulations.

The image has a 16:9 landscape layout and is an HD image with a resolution of 1920×1080 pixels at 300 dpi. This consistent image specification is maintained across all evaluations to ensure fair comparison and to obtain clearer, more reliable results.

https://doi.org/10.31436/iiumej.v27i2.4246

Figure 7. Sample of clean and actual size of the star image

Figure 8(a)-(d) shows the selected data of 4 images, and Table 3 presents the SNR values for each image. For clarity, each figure has been cropped and zoomed from the original test images to allow detailed visual inspection of the star blobs and their distortions under the different noise conditions. The actual image sizes are shown in Figure 6.

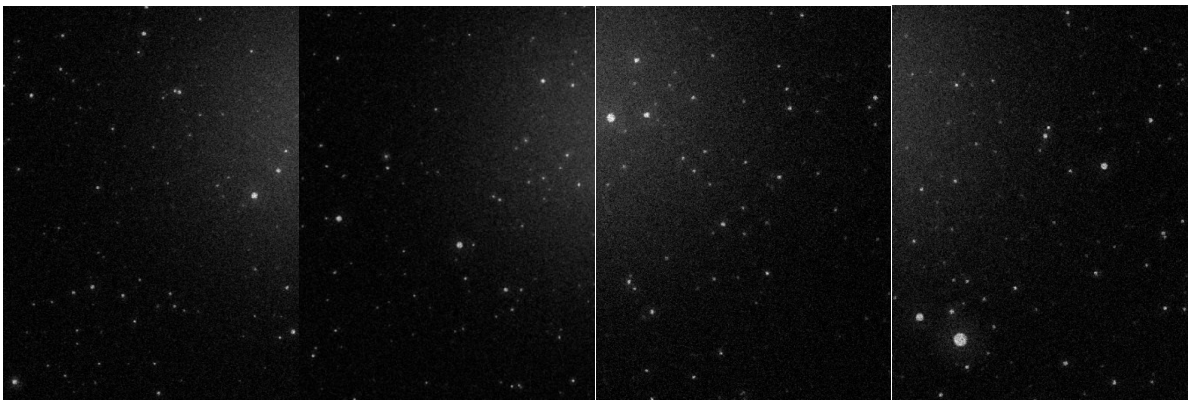

(a) Image 1 (b) Image 2 (c) Image 3 (d) Image 4

Figure 8. Selected star images in the dataset

Table 3. SNR of selected star images from the dataset

Image	**1**	**2**	**3**	**4**
SNR (dB)	-4.71	-2.09	0.72	0.53

In such conditions, the reflected starlight captured by a star sensor is often weak due to the absence of an atmosphere, harsh illumination contrast, and scattered light from the lunar regolith [11], [45], [46]. Therefore, testing under these SNR levels provides a realistic performance evaluation of the centroiding algorithm.

https://doi.org/10.31436/iiumej.v27i2.4246

4.2. Accuracy Analysis and Comparison

The proposed centroiding method is benchmarked against three established baselines, standard Center of Mass (COM), Gaussian fitting, and Sieve Search Algorithm (SSA), selected to span the design spectrum from purely intensity-weighted (COM) to model-fitting (Gaussian) to sub-region-search (SSA) approaches. Per-star localization accuracy is quantified using the Euclidean distance error (Eq. 4), which measures the straight-line distance between the detected centroid and its ground-truth position in pixel coordinates [47].

$$d = \sqrt{\left(x_i - x_i^{GT}\right)^2 + \left(y_i - y_i^{GT}\right)^2} \tag{4}$$

where GT is the coordinate of the ground truth. The comparison of position error or Euclidean distance is shown in graphs in Figures 9, 11, 13, and 15. The x-axis refers to the star count, where the count starts from the leftmost side of the star image until the rightmost side of the image. For reference, the actual star image size for the star count is shown in Figure 7.

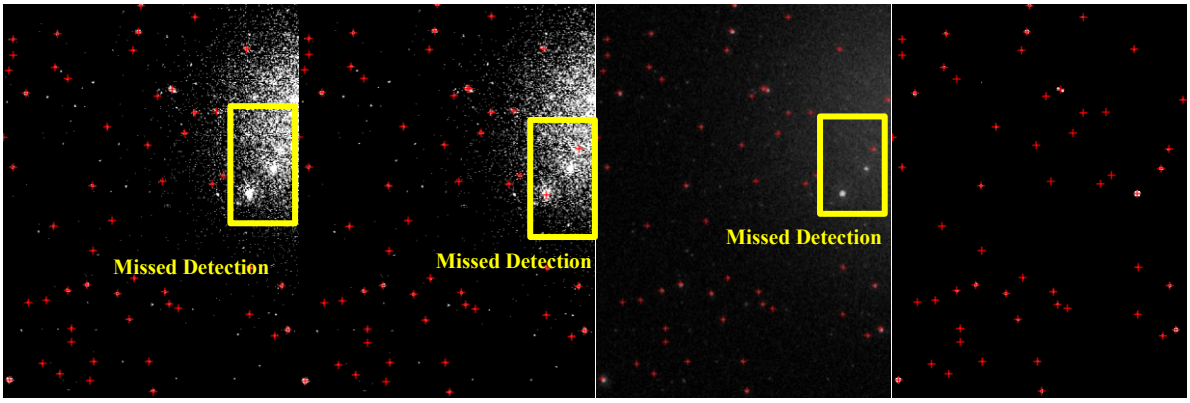

(a) Image 1 (b) Image 2 (c) Image 3 (d) Image 4

Figure 9. Centroiding results for Image 1 under an SNR of -4.71 dB. (a) The COM method shows several missed detections in dense star regions due to noise interference within the highlighted area. (b) Gaussian Fitting exhibits slightly improved centroid placement; however, some weak stars are still undetected under low SNR conditions. (c) SSA demonstrates better noise suppression yet misses several faint stars. (d) The proposed method successfully detects and locates more star centroids within the same region.

Figure 10 quantifies the visual differences observed in Figure 9. SSA exhibits the largest Euclidean distance among all methods, with errors exceeding 4 pixels in several stars. This is attributable to its sub-region search mechanism, which becomes unstable when the local intensity profile is dominated by noise rather than a clear stellar peak. All four methods show elevated errors on the right side of the frame (approaching 5 pixels) along with several missed detections; this region coincides with the highest local noise concentration in Image 1. The proposed algorithm, by combining median pre-filtering with intensity-weighted COM, retains most centroid errors below 1 pixel, indicating that the early impulse-noise suppression step protects the downstream centroid estimator from being skewed by spurious bright pixels.

https://doi.org/10.31436/iiumej.v27i2.4246

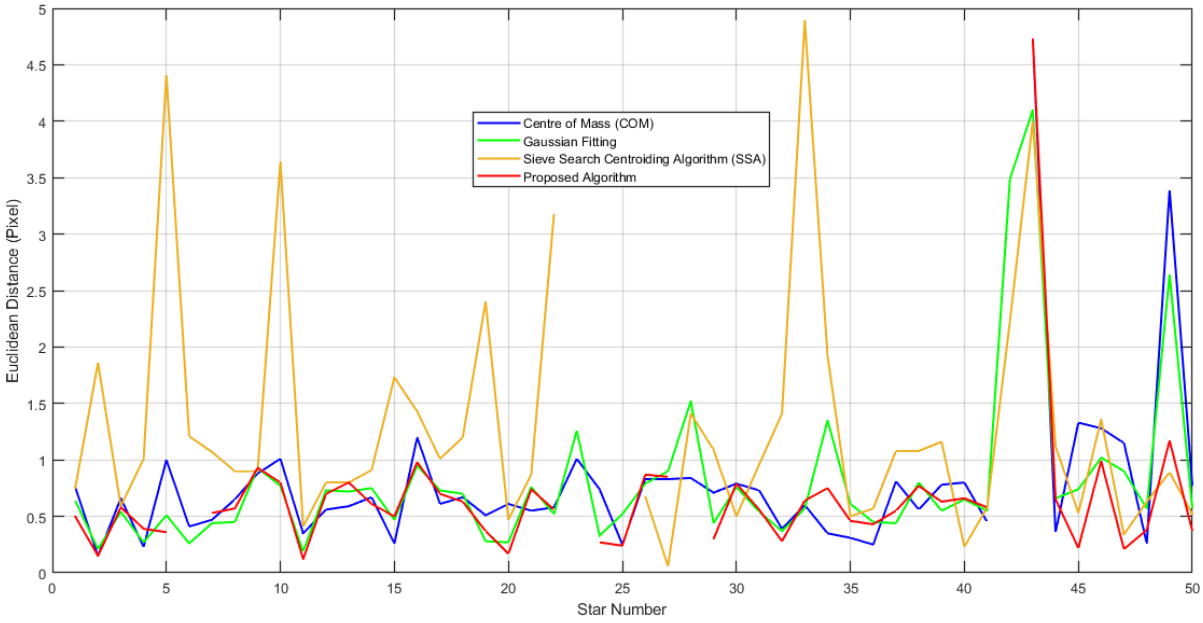

Figure 10. Comparison of Euclidean distance for each star in Image 1

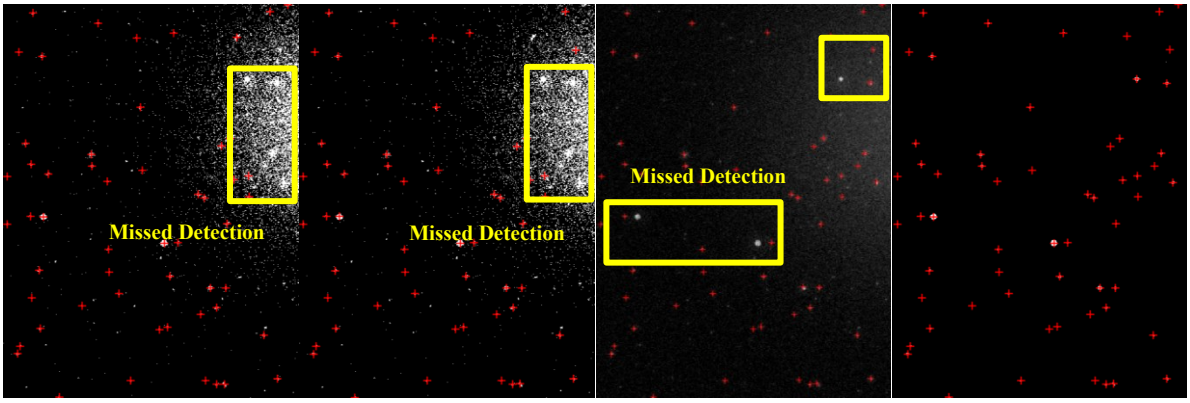

(a) Image 1 (b) Image 2 (c) Image 3 (d) Image 4

Figure 11. Centroiding results for Image 2 under an SNR of -2.09 dB. (a) The COM method shows poor detection in high-noise regions, with several missed centroids in the highlighted upper area. (b) Gaussian Fitting provides slightly better accuracy but still fails to detect faint stars affected by noise clustering. (c) SSA improves star localization, but multiple faint stars in both the upper and middle regions remain undetected. (d) The proposed method achieves the most stable detection by maintaining accurate centroid detection even in low-intensity regions.

Figure 12 shows that, at the marginally higher SNR of Image 2 (−2.09 dB), all methods produce errors in the 1–2 pixel range, but with markedly different reliability. SSA again records the largest positional errors and the highest number of missed stars, consistent with its known sensitivity to parameter choices when the local SNR is low. The proposed method, COM, and Gaussian fitting are within 0.5 pixels of each other for detected stars, but the proposed method detects the most true stars, indicating that the error reduction is achieved without sacrificing recall. This is a non-trivial property: many noise-suppression schemes improve precision by raising the detection threshold, which trades recall for accuracy.

https://doi.org/10.31436/iiumej.v27i2.4246

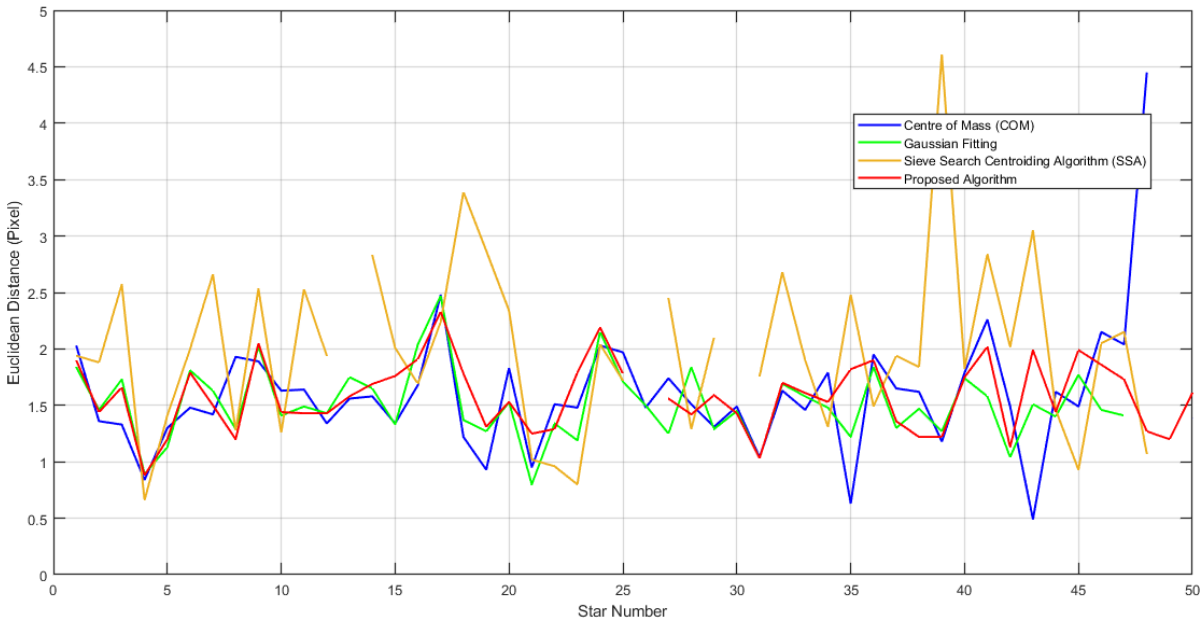

Figure 12. Comparison of Euclidean distance for each star in Image 2

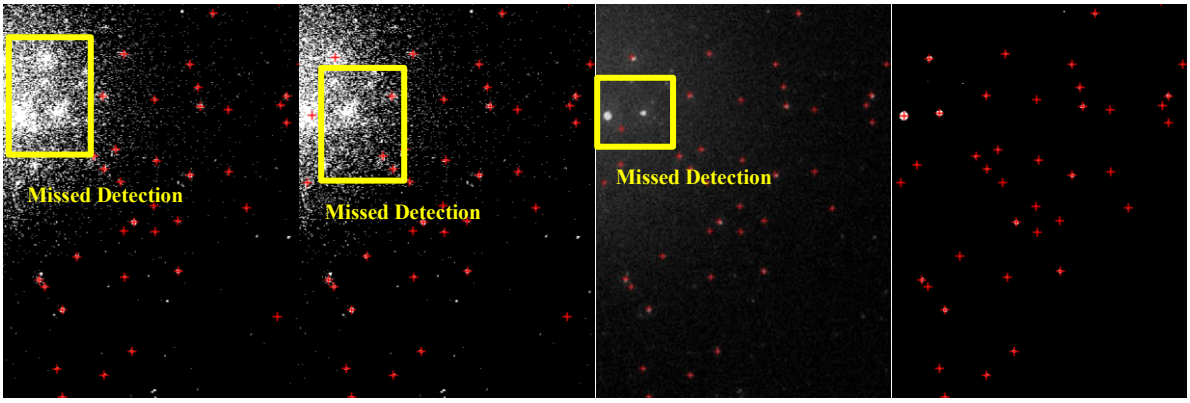

(a) Image 1 (b) Image 2 (c) Image 3 (d) Image 4

Figure 13. Centroiding results for Image 3 under an SNR of 0.72 dB. (a) The COM method exhibits centroid deviation in the upper-left region due to noise, leading to multiple missed detections. (b) Gaussian Fitting provides slightly improved localization but still fails to resolve faint stars affected by glare from sunlight. (c) SSA enhances centroid clarity but misses several faint stars within the noisy region. (d) The proposed method successfully detects the majority of visible stars with precise centroid placement, outperforming the other methods in maintaining centroid accuracy under moderate noise levels.

Image 3 introduces a spatially heterogeneous noise distribution, with degradation concentrated on the left side of the frame. Figure 14 mirrors this asymmetry: errors and missed detections cluster on the left and decrease monotonically toward the right. This pattern is informative because it isolates the methods' behavior in localized high-noise regions independent of the global SNR. The proposed algorithm keeps most centroid errors below 2 pixels even within the heavily corrupted region, while the baselines show abrupt error spikes. This robustness to spatially non-stationary noise is particularly relevant for lunar imaging, where solar-glare gradients produce exactly this kind of one-sided degradation.

https://doi.org/10.31436/iiumej.v27i2.4246

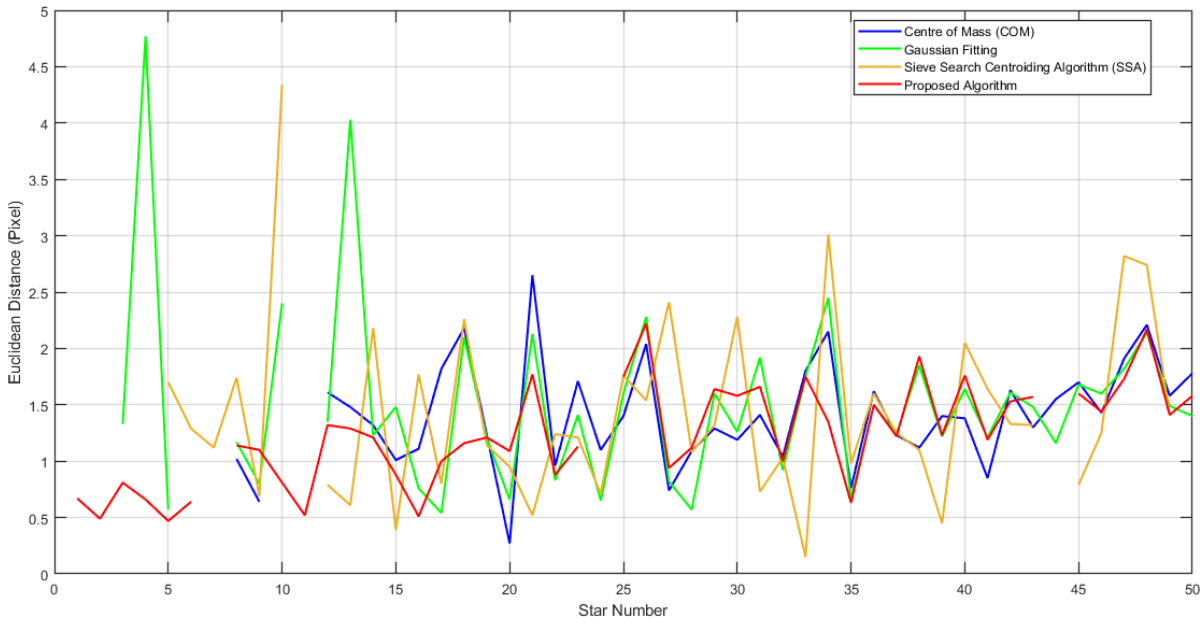

Figure 14. Comparison of Euclidean distance for each star in Image 3

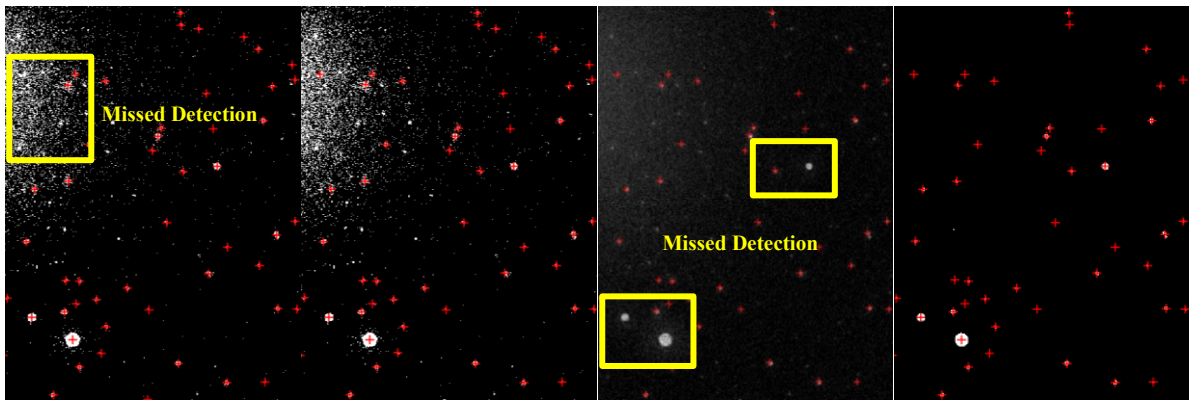

Figure 15. Centroiding results for Image 4 under an SNR of 0.53 dB. (a) The COM method provides good centroid placement with fewer missed detections; however, a few faint stars remain undetected near the noisy region. (b) The Gaussian Fitting method yields more stable centroiding than COM. (c) SSA exhibits multiple missed detections in a few regions, especially for faint stars. (d) The proposed algorithm effectively identifies most stars across the frame with minimal missed detections, demonstrating high robustness and accuracy in low-SNR imaging environments.

Figure 16 corresponds to Image 4, the most challenging case in the qualitative subset. All baselines exhibit position errors of approximately 4 pixels, which is an order of magnitude beyond the sub-pixel accuracy required for arc-second attitude determination. SSA exhibits a missed-detection pattern similar to Figure 13(c), suggesting that its sub-region search degrades systematically rather than gracefully under speckle and glare. Both Gaussian fitting and COM produce centroid errors that exceed those of the proposed method by 30–50%. Notably, the proposed algorithm's error distribution remains tight in this regime, indicating that the median-filter + thresholding combination effectively decouples the centroid estimator from the worst-case noise tail, rather than merely shifting the error distribution.

https://doi.org/10.31436/iiumej.v27i2.4246

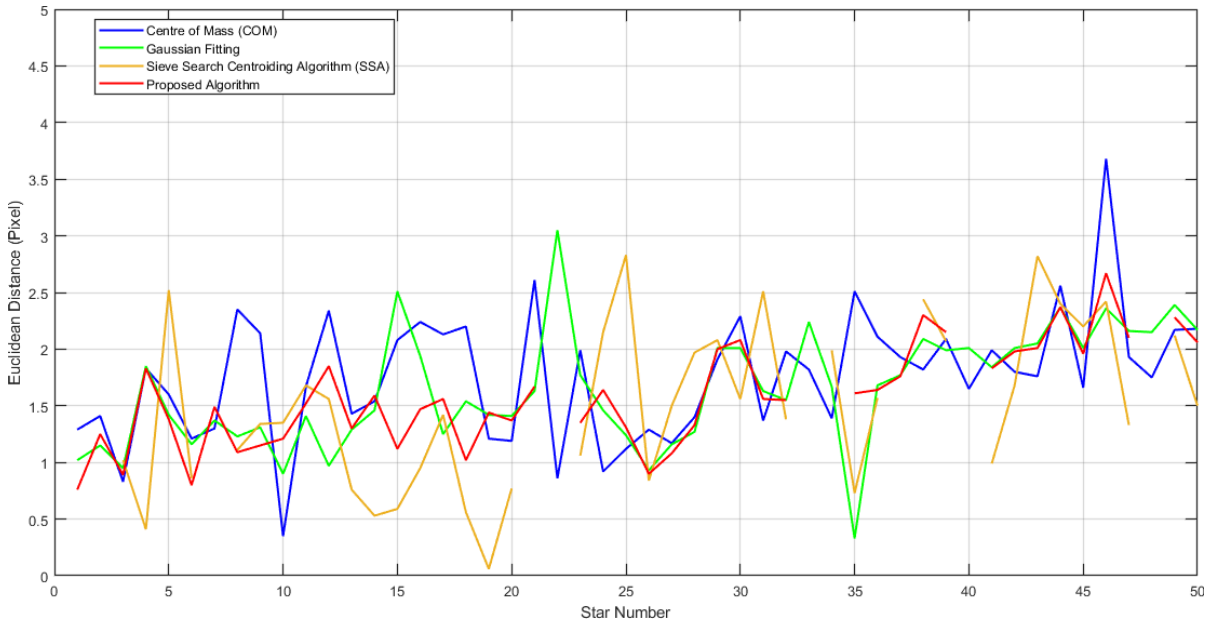

Figure 16. Comparison of Euclidean distance for each star in Image 4

To summarize the overall error performance for the star images, $RMSE$ is used to evaluate a statistical overview of error magnitude across all detected stars, as in Eq. (5) [48]:

$$RMSE = \sqrt{MSE} = \sqrt{\frac{1}{N}\sum_{i=1}^{N}(y_i - \hat{y}_i)^2} \tag{5}$$

where $e_i = y_i - \hat{y}_i$ is the Euclidean error that has been calculated, and N is the number of stars. This experiment is also extended to the remaining 26 star field images to obtain a more comprehensive set of results for evaluation. The performance results for all methods on every 30 images are shown in Figure 17.

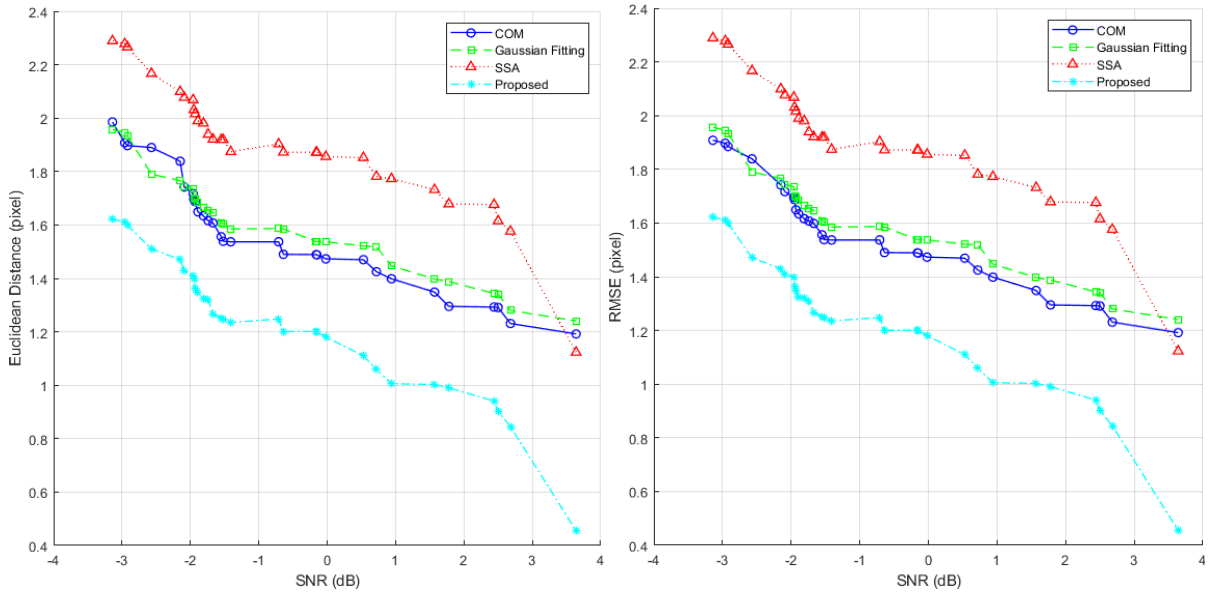

(a) Euclidean Distance (b) RMSE

Figure 17. Performance comparison between existing methods and the proposed method

Aggregating across all 30 images (Figure 17) reveals a consistent ranking: SSA records the highest position error, followed by Gaussian fitting, then standard COM, with the proposed method producing the lowest values on both Euclidean distance and RMSE axes. Importantly, the gap between the proposed method and the next-best baseline widens as the average noise level increases, indicating that the advantage is most pronounced precisely in the operating regime that lunar missions encounter. To complement positional accuracy, detection reliability is quantified using the false detection rate (FDR), which is critical because false centroids contaminate the subsequent star-identification stage of a star tracker. A higher FDR indicates over-sensitivity to noise, while a lower FDR reflects more reliable detection [27]. The FDR can be expressed as in Eq. (6):

$$FDR = \frac{N_{false}}{N_{detected}} \times 100\% \quad (6)$$

Table 4 presents the quantitative comparison of the average centroiding accuracy and reliability among the four tested methods.

Table 4. Summary of the accuracy analysis of the average of the proposed method with other methods

Methods	RMSE	Euclidean Distance	False Detection Rate (%)
Center of Mass (COM)	1.551	1.373	13.949
Gaussian Fitting	1.599	1.368	9.983
Sieve Search Algorithm (SSA)	1.904	1.679	12.637
Proposed Algorithm	1.218	1.143	6.716

Three observations emerge from Table 4. First, the proposed method achieves the lowest values on every metric simultaneously: RMSE = 1.218 pixels (a 21.5% reduction over the best baseline, COM at 1.551), Euclidean distance error = 1.143 pixels (a 16.4% reduction over Gaussian fitting at 1.368), and FDR = 6.716% (a 32.7% reduction over Gaussian fitting at 9.983%). Joint dominance in both accuracy and reliability is uncommon in the literature, where most low-complexity methods improve one metric at the expense of the other. Second, SSA underperforms standard COM on every metric in this evaluation, despite its design objective of improved noise robustness. This is consistent with prior reports that SSA's sub-region partitioning is sensitive to parameter selection and degrades on noise-dominated, sparse star fields, which differ from the dense fields for which it was originally tuned. Third, Gaussian fitting yields a competitive Euclidean distance (1.368 pixels, second-best) but is penalized by a higher RMSE (1.599 pixels), indicating that its error distribution has a heavier tail; that is, when it fails, it fails badly. The proposed method's tighter RMSE–Euclidean gap suggests a more uniform error distribution and therefore more predictable behavior, a desirable property for safety-critical onboard navigation. Practically, the observed FDR of 6.716% means that fewer than 1 in 14 detected centroids is spurious, which is within the tolerance of standard star-identification algorithms (typically robust to FDR below ~10%).

Taken together, the per-image and aggregate results consistently show that the proposed pipeline delivers a favorable accuracy–reliability–complexity trade-off. The improvement is not driven by a single metric or a single noise model, but is observed across all five degradation types and the full SNR range tested. Two limitations of this study should, however, be acknowledged. First, the noise models are statistical surrogates for lunar imaging conditions; physics-based models that incorporate the camera point-spread function (PSF), pixel response

non-uniformity (PRNU), and dark-current shot noise would yield more realistic error estimates. Second, runtime profiling of representative spaceflight processors (e.g., FPGAs, DSPs) was outside the scope of this paper. Both limitations directly motivate the future work outlined in Section 5.

5. CONCLUSION

This paper presented a low-complexity yet robust star centroiding algorithm tailored to the demanding noise environment of lunar surface navigation. The pipeline integrates three deliberately simple components — 3×3 median filtering for impulse-noise suppression, an adaptive global threshold fixed at 30% of peak intensity for star segmentation, and an intensity-weighted center-of-mass estimator for sub-pixel localization — into a fully MATLAB-replicable workflow. Validated on 30 Stellarium-derived star fields corrupted by Gaussian, Poisson, salt-and-pepper, speckle, and synthetic solar-glare noise, the proposed method outperformed three established baselines (standard COM, Gaussian fitting, and SSA) on every aggregate metric: it achieved an average RMSE of 1.218 pixels (a 21.5% reduction over the best baseline), an average Euclidean distance error of 1.143 pixels (a 16.4% reduction), and a false detection rate of 6.716% (a 32.7% reduction). Crucially, this dominance was consistent across all noise models and all SNR levels tested, indicating that the gains arise from the pipeline's architecture rather than from tuning to a specific scenario. The algorithm therefore advances the state of the art on the accuracy–reliability–complexity Pareto frontier and is well-suited to the resource-constrained processors typical of lunar landers, rovers, and CubeSat-class spacecraft.

Four directions for future work are identified. First, hardware deployment and runtime characterization on Field-Programmable Gate Arrays (FPGAs), Digital Signal Processors (DSPs), and CubeSat-class edge platforms will quantify the algorithm's achievable frame rate, power envelope, and timing determinism, complementing the present accuracy-only evaluation. Second, the statistical noise models used here will be augmented with physics-based degradation models that incorporate the optical point spread function (PSF), CMOS pixel response non-uniformity (PRNU), dark-current shot noise, and rad-hardened sensor effects to better predict in-flight performance. Third, an end-to-end star-camera calibration pipeline will be developed to enable real-time star acquisition under real night-sky conditions and to support a Lost-in-Space (LIS) operating mode in which the system autonomously identifies stars without prior attitude information. Fourth, the pipeline will be evaluated on representative lunar mission imagery (e.g., Chang'e and Yutu-2 datasets) to assess generalization beyond the simulated benchmarks reported here. Together, these steps will progress the proposed algorithm from a validated software prototype toward a deployable component of an autonomous lunar navigation system.

ACKNOWLEDGMENT

This research was supported by the Ministry of Higher Education of Malaysia (MOHE) Fundamental Research Grant Scheme (FRGS) code number FRGS/1/2024/TK07/UIAM/02/1 and supported by KHAIR Award Fund from the Center for Postgraduate Studies (CPS) IIUM.

REFERENCES

[1] F. Wu *et al.*, "Anti-noise Star Image Extraction Algorithm for Star Trackers Based on YOLOv5," in *2023 Intelligent Methods, Systems, and Applications (IMSA)*, 2023, pp. 149–154. doi: 10.1109/IMSA58542.2023.10217394.

[2] Anqi Fan, "China-russia lunar base collaboration 'A perfect match.' ," Global Times.

[3] B. Yağlioğlu, B. B. İnaltekin, and M. Gökten, "The First Turkish Lunar Mission Part 1: Programmatic, Mission and System Aspects," in *2023 10th International Conference on Recent Advances in Air and Space Technologies (RAST)*, IEEE, Jun. 2023, pp. 1–6. doi: 10.1109/RAST57548.2023.10197907.

[4] B. B. İnaltekin, B. Yağlioğlu, and M. Ceylan, "The First Turkish Lunar Mission Part 2: Overview of Space Segment," in *2023 10th International Conference on Recent Advances in Air and Space Technologies (RAST)*, IEEE, Jun. 2023, pp. 1–5. doi: 10.1109/RAST57548.2023.10197853.

[5] M. B. Trageser and D. G. Hoag, "Apollo Spacecraft Guidance System," *IFAC Proceedings Volumes*, vol. 2, no. 1, pp. 435–463, Jun. 1965, doi: 10.1016/S1474-6670(17)69119-5.

[6] C. Li *et al.*, "Overview of the Chang'e-4 Mission: Opening the Frontier of Scientific Exploration of the Lunar Far Side," *Space Sci. Rev.*, vol. 217, no. 2, p. 35, Mar. 2021, doi: 10.1007/s11214-021-00793-z.

[7] Q. Wang and J. Liu, "A Chang'e-4 mission concept and vision of future Chinese lunar exploration activities," *Acta Astronaut.*, vol. 127, pp. 678–683, Oct. 2016, doi: 10.1016/j.actaastro.2016.06.024.

[8] B. Wang, H. Wang, and Z. Jin, "An Efficient and Robust Star Identification Algorithm Based on Neural Networks," *Sensors*, vol. 21, no. 22, p. 7686, Nov. 2021, doi: 10.3390/s21227686.

[9] Q. Zhao, J. Liao, D. Zhang, and J. Feng, "Grayscale Iterative Star Spot Extraction Algorithm Based on Image Entropy," *Applied Sciences*, vol. 14, no. 20, p. 9207, Oct. 2024, doi: 10.3390/app14209207.

[10] D. E. Wilhelms, J. F. McCauley, and N. J. Trask, "The geologic history of the Moon," 1987. doi: 10.3133/pp1348.

[11] H. Lin *et al.*, "Photometric properties of lunar regolith revealed by the Yutu-2 rover," *Astron. Astrophys.*, vol. 638, p. A35, Jun. 2020, doi: 10.1051/0004-6361/202037859.

[12] R. Li *et al.*, "Cone penetration resistance of CUMT-1 lunar regolith simulant under magnetic-similitude lunar gravity condition," *Acta Geotech.*, vol. 18, no. 12, pp. 6725–6744, Dec. 2023, doi: 10.1007/s11440-023-01971-9.

[13] NASA, "Moon Composition & Structure." Accessed: Oct. 03, 2025. [Online]. Available: https://science.nasa.gov/moon/composition/

[14] Y.-L. Zou, J.-Z. Liu, J.-J. Liu, and T. Xu, "Reflectance Spectral Characteristics of Lunar Surface Materials," *Chinese Journal of Astronomy and Astrophysics*, vol. 4, no. 1, pp. 97–104, Feb. 2004, doi: 10.1088/1009-9271/4/1/97.

[15] M. Horányi, J. R. Szalay, and X. Wang, "The lunar dust environment: concerns for Moon-based astronomy," *Philosophical Transactions of the Royal Society A: Mathematical, Physical and Engineering Sciences*, vol. 382, no. 2271, May 2024, doi: 10.1098/rsta.2023.0075.

[16] J. J. Rennilson and D. R. Criswell, "Surveyor observations of lunar horizon-glow," *The Moon*, vol. 10, no. 2, pp. 121–142, Jun. 1974, doi: 10.1007/BF00655715.

[17] NASA, "The Apollo Lunar Surface Journal and Apollo Flight Journal." Accessed: Nov. 23, 2025. [Online]. Available: https://www.nasa.gov/history/alsj-and-afj/

[18] Rafael Alanis, "Diviner Global Composition," NASA Science. Accessed: Dec. 04, 2025. [Online]. Available: https://science.nasa.gov/photojournal/diviner-global-composition/

[19] C. C. Liebe, "Accuracy performance of star trackers - a tutorial," *IEEE Trans. Aerosp. Electron. Syst.*, vol. 38, no. 2, pp. 587–599, Apr. 2002, doi: 10.1109/TAES.2002.1008988.

[20] F. N. Chukhovskii, P. V. Konarev, and V. V. Volkov, "Denoising of the Poisson-Noise Statistics 2D Image Patterns in the Computer X-ray Diffraction Tomography," *Crystals (Basel).*, vol. 13, no. 4, p. 561, Mar. 2023, doi: 10.3390/cryst13040561.

[21] R. K. Painam and M. Suchetha, "Comparative Performance Analysis of Spatial Domain Filters for Removing Speckle Noise in SAR images," in *2022 First International Conference on Electrical, Electronics, Information and Communication Technologies (ICEEICT)*, IEEE, Feb. 2022, pp. 01–05. doi: 10.1109/ICEEICT53079.2022.9768585.

[22] S. V. Parhad, K. K. Warhade, and S. S. Shitole, "Speckle noise reduction in sar images using improved filtering and supervised classification," *Multimed. Tools Appl.*, vol. 83, no. 18, pp. 54615–54636, Dec. 2023, doi: 10.1007/s11042-023-17648-0.

[23] W. Xu, Y. Liang, W. Chen, and F. Wang, "Recent advances of stretched Gaussian distribution underlying Hausdorff fractal distance and its applications in fitting stretched Gaussian noise," *Physica A: Statistical Mechanics and its Applications*, vol. 539, Feb. 2020, doi: 10.1016/j.physa.2019.122996.

[24] O. O. Khalifa, *Digital Image Processing and Computer Vision : Fundamentals and Applications*. IIUM Press, 2021.

[25] Y. Fan, H. Xiao, W. Cao, L. Zuo, and S. Chen, "FPGA Implementation of Real-time Star Centroid Extraction Algorithm," in *2019 IEEE 2nd International Conference on Information Communication and Signal Processing (ICICSP)*, 2019, pp. 395–399. doi: 10.1109/ICICSP48821.2019.8958483.

[26] Z. Mahi, M. S. Karoui, and M. Keche, "A Non-Stellar Big Bright Object Elimination and Star Centroid Extraction Algorithm for Star Tracker," in *2024 IEEE Mediterranean and Middle-East Geoscience and Remote Sensing Symposium (M2GARSS)*, 2024, pp. 1–5. doi: 10.1109/M2GARSS57310.2024.10537475.

[27] Z. Mahi and M. S. Karoui, "A Comparative Study of Star Detection Methods for a Satellite-Onboard Star Tracker," in *2019 International Conference on Advanced Electrical Engineering (ICAEE)*, 2019, pp. 1–6. doi: 10.1109/ICAEE47123.2019.9015160.

[28] M. Ceresoli, F. Maccari, E. Moresi, and M. Lavagna, "Design and station-keeping strategies for robust lunar navigation constellations," *Acta Astronaut.*, vol. 236, pp. 20–31, Nov. 2025, doi: 10.1016/j.actaastro.2025.06.025.

[29] F. Xing, Y. Dong, Z. You, and Q. Zhou, "APS star tracker and attitude estimation," in *2006 1st International Symposium on Systems and Control in Aerospace and Astronautics*, 2006, pp. 5 pp. – 38. doi: 10.1109/ISSCAA.2006.1627697.

[30] H. Cai, Z. Yang, X. Cao, W. Xia, and X. Xu, "A new iterative triclass thresholding technique in image segmentation," *IEEE Transactions on Image Processing*, vol. 23, no. 3, pp. 1038–1046, Mar. 2014, doi: 10.1109/TIP.2014.2298981.

[31] H. Liang, H. Jia, Z. Xing, J. Ma, and X. Peng, "Modified Grasshopper Algorithm-Based Multilevel Thresholding for Color Image Segmentation," *IEEE Access*, vol. 7, pp. 11258–11295, 2019, doi: 10.1109/ACCESS.2019.2891673.

[32] R. C. Gonzalez and R. E. Woods, *Digital Image Processing, 4th ed.*, 4th ed. Pearson, 2018.

[33] R. Raman, V. Kumar, B. G. Pillai, D. Rabadiya, S. Patre, and R. Meenakshi, "Brain Image Denoising and Segmentation Using Advanced Mixed Thresholding and Edge Preservation Analysis Technique," in *2024 International Conference on Knowledge Engineering and Communication Systems (ICKECS)*, IEEE, Apr. 2024, pp. 1–5. doi: 10.1109/ICKECS61492.2024.10617270.

[34] A. H. Razaman, Y. A. Ahmad, T. S. Gunawan, and O. O. Khalifa, "The Noise Reduction Algorithm for Star Detection," *PERINTIS EJournal*, vol. 15, no. 2, pp. 37–46, 2025, doi: 10.5281/zenodo.1808125.

[35] C. Chen, Q. Chen, C. Gao, N. Zhang, X. Wang, and Y. Zhai, "Method of Blob detection based on radon transform," in *2018 Chinese Control And Decision Conference (CCDC)*, 2018, pp. 5762–5767. doi: 10.1109/CCDC.2018.8408138.

[36] J. R. Janesick, *Scientific Charge-Coupled Devices*. SPIE, 2001. doi: 10.1117/3.374903.

[37] A. H. Razaman, Y. A. Ahmad, O. O. Khalifa, N. Saidin, and A. W. Azman, "Review Paper on Centroiding Algorithm for Lunar Navigation," in *2025 21st IEEE International Colloquium on Signal Processing & Its Applications (CSPA)*, IEEE, Feb. 2025, pp. 89–93. doi: 10.1109/CSPA64953.2025.10933304.

[38] V. C. Karaparambil, N. S. Manjarekar, and P. M. Singru, "Sieve Search Centroiding Algorithm for Star Sensors," *Sensors*, vol. 23, no. 6, 2023, doi: 10.3390/s23063222.

[39] "Stellarium Web Online Star Map," 2025. [Online]. Available: https://stellarium-web.org/

[40] M.-H. Hung, J.-S. Pan, and C.-H. Hsieh, "A fast algorithm of temporal median filter for background subtraction," *Journal of Information Hiding and Multimedia Signal Processing*, vol. 5, pp. 33–40, Jun. 2014.

[41] Patrice, "Patrice's Lectures: COMPSCI 373 Image Filtering [Course Presentation]," in *The University of Auckland*, 2016. Accessed: Apr. 26, 2025. [Online]. Available: https://www.cs.auckland.ac.nz/courss/compsci373s1c/PatricesLectures/

[42] Z. Mahi, M. S. Karoui, and M. Keche, "A new star detection algorithm based on the combination of thresholding and filtering technique," in *2022 7th International Conference on Image and Signal Processing and their Applications (ISPA)*, IEEE, May 2022, pp. 1–6. doi: 10.1109/ISPA54004.2022.9786030.

[43] R. Singh, C. Prabha, and S. Abdulla, "Optimized CNN framework for malaria detection using Otsu thresholding−based image segmentation," *Sci. Rep.*, vol. 15, no. 1, p. 40117, Nov. 2025, doi: 10.1038/s41598-025-23961-5.

[44] X. Qian, H. Yu, and S. Chen, "A Global-Shutter Centroiding Measurement CMOS Image Sensor With Star Region SNR Improvement for Star Trackers," *IEEE Transactions on Circuits and Systems for Video Technology*, vol. 26, no. 8, pp. 1555–1562, 2016, doi: 10.1109/TCSVT.2015.2469091.

[45] R. M. Marshal, O. Rüsch, C. Wöhler, K. Wohlfarth, and S. Velichko, "Photometry of LROC NAC resolved rock-rich regions on the Moon," *Icarus*, vol. 394, p. 115419, Apr. 2023, doi: 10.1016/j.icarus.2022.115419.

[46] S. Velichko, V. Korokhin, Y. Shkuratov, V. Kaydash, Y. Surkov, and G. Videen, "Photometric analysis of the Luna spacecraft landing sites," *Planet. Space Sci.*, vol. 216, p. 105475, Jul. 2022, doi: 10.1016/j.pss.2022.105475.

[47] P.-E. Danielsson, "Euclidean distance mapping," *Computer Graphics and Image Processing*, vol. 14, no. 3, pp. 227–248, Nov. 1980, doi: 10.1016/0146-664X(80)90054-4.

[48] Akshita Chugh, "MAE, MSE, RMSE, Coefficient of Determination, Adjusted R Squared — Which Metric is Better?," Medium. Accessed: Sep. 19, 2025. [Online]. Available: https://medium.com/analytics-vidhya/mae-mse-rmse-coefficient-of-determination-adjusted-r-squared-which-metric-is-better-cd0326a5697e